Optical Materials 159 (2025) 116654

Contents lists available at ScienceDirect

Optical Materials

journal homepage: www.elsevier.com/locate/optmat

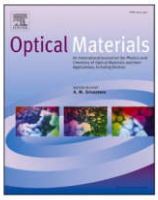

Research Article

Photoelectrochemical BiSI-based visible light detector

Evgeny Bondarenko [a], Anatoly I. Kulak [b], Alexander V. Mazanik [c,d,*], Ivan A. Svito [c], Eugene Streltsov [e]

[a] Faculty of Chemistry, Department of Physical Chemistry and Technology of Polymers, Silesian University of Technology, Strzody 9, 44-100, Gliwice, Poland
[b] Institute of General and Inorganic Chemistry, National Academy of Sciences of Belarus, Surganov St. 9/1, 220072, Minsk, Republic of Belarus
[c] Department of Solid State Physics and Nanotechnologies, Faculty of Physics, Belarusian State University, 4, Nezavisimosti Av., 220030, Minsk, Republic of Belarus
[d] Institute of Power Engineering, National Academy of Sciences of Belarus, Akademicheskaya St. 15/2, 220072, Minsk, Republic of Belarus
[e] Department of Physical Chemistry and Electrochemistry, Faculty of Chemistry, Belarusian State University, 4, Nezavisimosti Av., 220030, Minsk, Republic of Belarus

ARTICLE INFO

Keywords:
BiSI
Chemical bath deposition
Photoelectrochemical photodetector

ABSTRACT

We suggest a photoelectrochemical detector based on semiconductor bismuth thioiodide BiSI with the band gap energy E_g = 1.59 eV (direct optical transitions). The bismuth thioiodide was synthesized by the chemical bath deposition on a conductive FTO glass. The structure of BiSI film represents randomly oriented needle-like single crystals. The nucleation and growth of needle-like BiSI single crystals from a single center and the absence of inter-crystallite boundaries provide a high external quantum efficiency of photocurrent up to 52 % at 400 nm. It corresponds to ampere-watt responsivity of 0.16 A/W. BiSI photodetector possesses a high specific detectivity of $3.4 \bullet 10^{11}$ cm•$Hz^{1/2}$/W and an on/off time equal to 26/435 ms. In aqueous electrolyte containing both S^{2-} and I^- anions, the photodetector is characterized by a high temporal stability of photocurrent and cyclability (thousands of cycles) under visible light illumination.

1. Introduction

Photodetectors are the devices, which convert light into electrical signal. They are widely used in fiber optic lines and waveguides [1–3], lasers [4], light modulators [5–7], light intensity measurements [8,9] and many other optoelectronic applications [10–12]. The functioning of photodetectors is based on the separation of the photocharges generated under illumination. As the rule, the charge separation occurs in *p-n* junction [13–18], heterojunction with other semiconductor [19,20] or interface with a solution [21,22].

For photodetectors designing, the various semiconducting materials are employed: Si [23,24], Ge [25,26], binary semiconductor compounds $A^{III}B^{V}$ [27,28], $A^{II}B^{VI}$ [29]. A special group is formed by semiconducting bismuth compounds: chalcogenides (Bi_2S_3, Bi_2Se_3, Bi_2Te_3 [30–32]), oxyhalides (BiOCl, BiOBr, BiOI [33–35]), thiohalides (BiSI, BiSeI, $Bi_{13}S_{18}I_2$ [36–38]), etc.

A great interest in semiconducting bismuth compounds is due to relatively simple methods of their synthesis, the possibility of wide range variation of the band gap energy and the range of spectral sensitivity by changing their composition, as well as obtaining thin films and various nanostructures (nanocrystals, nanowires, nanorods, nanotubes, nanobelts, nanosheets). In addition, these semiconductors are characterized by high light absorption coefficients and are non-toxic. As a high-Z element, bismuth has a potential for application of its semiconductor compounds for detection of X-ray and gamma quanta [39].

Recently, there has been a report of the first solid state photodetector based on BiSI thin films [40]. Due to band gap energy E_g = 1.57 eV (direct optical transitions), this semiconductor strongly absorbs the visible light having light absorption coefficient up to $5 \cdot 10^4$ cm^{-1} at 600 nm [41]. For the synthesis of bismuth thioiodide, a multistage method was proposed, which includes the conversion of BiI_3 to BiOI by hydrolysis [42]. Further, BiOI was converted into BiSI due to the treatment of crystallites with gaseous H_2S at high temperature. A certain disadvantage of this method, along with its multi-stage nature, is the application of a gas hazardous to human health. In addition, during the decomposition of H_2S, the formation of elemental sulfur is possible, which, being deposited on the surface of crystallites, forms dielectric particles that impede the transport of photocharges.

To date, various methods for the synthesis of BiSI are known. In particular, bismuth thioiodide single crystals can be obtained by the

* Corresponding author. Department of Solid State Physics and Nanotechnologies, Faculty of Physics, Belarusian State University, 4, Nezavisimosti Av., 220030, Minsk, Republic of Belarus.
E-mail address: mazanikalexander@gmail.com (A.V. Mazanik).

https://doi.org/10.1016/j.optmat.2025.116654
Received 20 June 2024; Received in revised form 30 December 2024; Accepted 7 January 2025
Available online 9 January 2025

vapor deposition by the heating a mixture of bismuth, sulfur and iodine at a low pressure [43]. Solvothermal synthesis is used to obtain polycrystalline BiSI powders [39,44–47] by heating of aqueous [39,44–46], ethanol [46,47] or ethyleneglycol [39] solutions containing precursors of bismuth ($BiCl_3$ [44–46], BiI_3 [46], Bi_2S_3 [39,46], $Bi(NO_3)_3$ [47]), iodine (I_2 [39,44,45,47], BiI_3 [46], NaI [46]) and sulfur (thiourea [44–47], S [46], Bi_2S_3 [39,46]).

A separate important task in the preparation of semiconductor electrodes is their deposition onto a transparent conductive substrate and the formation of high-quality ohmic contacts. Therefore, the development of new single-stage and environmentally friendly methods for the synthesis of BiSI on transparent conductive substrates is very topical.

In this work, we propose a one-step method for chemical deposition of BiSI grown as a set of needle-shaped single crystals randomly oriented relative to each other directly on conductive substrates. The prepared BiSI-based photoelectrochemical (PEC) detector possesses sensitivity in a visible range with the responsivity up to 0.16 A/W at 400 nm, high specific detectivity ($3.4 \bullet 10^{11}$ cm$\bullet$Hz$^{1/2}$/W), and on/off time equal to 26/435 ms.

2. Experimental section

2.1. Materials and synthesis

For BiSI deposition, TEC-7 8 Ohm/sq FTO glasses (Great Cell Solar materials, Australia) were cut into pieces 0.7 × 2.0 cm^2. Before deposition, the substrates were degreased with a detergent and then chemically cleaned in a boiling mixture of aqueous ammonia (25 %) and hydrogen peroxide (30 %) in a volume ratio of 5:1. After boiling out of the ammonia, the samples were washed with distilled water and air-dried.

The chemical bath deposition (CBD) of semiconductors from solutions allows formation of crystallites of various sizes and shapes by crystallization of a substance directly on the surface of both conductive and dielectric substrates. The CBD method provides a tight contact of crystallites both with the substrate and with each other. The deposition rate of semiconductors is usually controlled by such parameters as the concentration of substances in solution and its temperature [48]. A convenient approach to control the rate of precipitate formation is the binding of metal cations into stable complexes preventing "instantaneous" precipitation in the presence of all components (precursors) in the solution.

In our experiments, the solution for BiSI deposition contained 0.01 M $Bi(NO_3)_3$, 0.1 M of thiourea, 0.015 M KI and 0.1 M HNO_3. The BiSI crystals were grown by immersion of clean FTO substrates into solution and keeping them at 85 °C for 2 h. We used the binding of bismuth cations Bi^{3+} into stable chelate complexes with thiourea:

$$Bi^{3+} + n(CS(NH_2)_2) \rightarrow Bi(CS(NH_2)_2)_n^{3+}. \quad (1)$$

In the presence of iodide anions in an aqueous solution, the complex is destroyed and a poorly soluble BiSI precipitate is formed:

$$Bi[CS(NH_2)_2]_n^{3+} + 2H_2O + I^- \rightarrow BiSI\downarrow + (n\text{-}1)CS(NH_2)_2 + H_2CN_2 + 2H_3O^+. \quad (2)$$

The complex formation (Eq. (1)) took place in an acidic medium, since nitric acid was added to prevent the hydrolysis of $Bi(NO_3)_3$. This made it possible to obtain BiSI precipitate that does not contain the crystalline phases of basic bismuth salts.

After deposition, the samples were allowed cooling, washed with water and air-dried.

2.2. Structural characterization

Phase composition was identified by the X-ray diffraction (XRD) analysis using a D8 ADVANCE diffractometer (Bruker, Germany) equipped with a Cu Kα source with a Ni filter. The scan range was 10–90° and the rate was 0.5°/min. As a reference for phases identification, the JCPDS database was employed.

The surface morphology of the bismuth thioiodide films was studied using a LEO 1455 VP Scanning Electron Microscope (Zeiss, Germany). The selected area electron diffraction (SAED) was registered with an EM 912 transmission electron microscope (Zeiss, Germany).

Raman spectra were recorded using a Nanofinder HE confocal spectrometer (LOTIS TII, Belarus-Japan) with a 532 nm solid-state laser as an excitation source. The incident optical power was attenuated down to 20 μW for minimization of thermal impact. The backscattered light without analysis of its polarization was dispersed with a 600 lines/mm diffraction grating that provided a spectral resolution better than 2.5 cm^{-1} and registered with a cooled silicon charge coupled device. The signal acquisition time was equal to 60 s. The spectrum calibration was done using a built-in gas discharge lamp that provided accuracy better than 2.5 cm^{-1}.

2.3. Evaluation of electrical conductivity

To estimate the electrical conductivity of an individual BiSI needle, the dark current-voltage (I–V) curves were measured using a microprobe station and a Keithley 2600B source-meter. Tungsten probes with a tip diameter of 1 μm were used in these experiments. The measurements were carried out in the two-probe mode, when one tip was pressed to the FTO substrate and the other to a single BiSI crystal grown on its surface.

2.4. Photoelectrochemical characterization

Cyclic voltammograms and current transients were recorded in a three-electrode electrochemical cell (Fig. 1). The Pt wire was used as a counter electrode (CE). The saturated Ag,AgCl|KCl electrode (+0.201 V vs. SHE) was used as reference (RE). The BiSI electrode and the reference electrode were separated using a salt bridge, filled with 0.5 M K_2SO_4 solution. The potential scan rate during all experiments comprised 5 mV/s. The 10 W blue 465 nm light emission diode (LED) was used as a light source in these experiments. Light intensity was measured using a

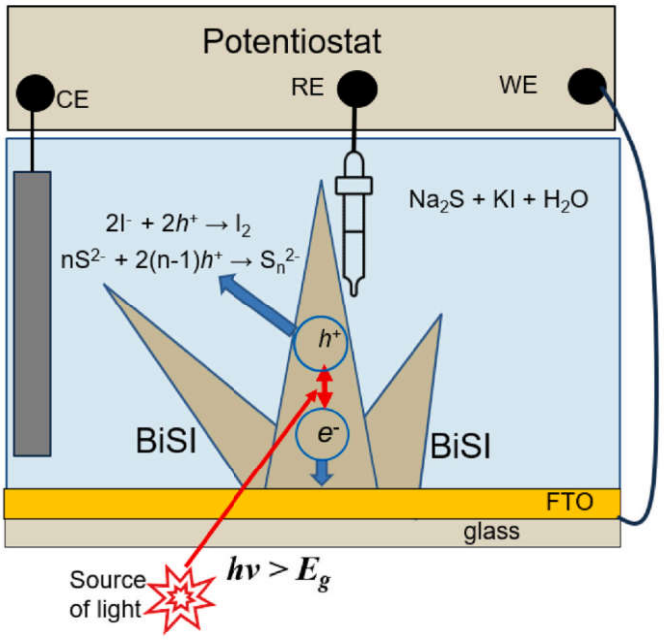

Fig. 1. Sketch of the experimental setup for characterization of the PEC behavior of BiSI photoelectrodes.

calibrated OPT101 photodiode (Texas Instruments, USA) and comprised 1.2 mW/cm^2. The BiSI samples (working electrode – WE) were illuminated from the glass side. To prevent a light absorption by the solutions, the samples were stacked on the wall of a flat rectangular electrochemical cell. The incident light was modulated with a frequency of 0.3 Hz for separation the dark current and photocurrent.

For registration of spectral dependences of photosensitivity, a grating monochromator (1 nm slit bandwidth) equipped with a 250 W halogen lamp and filters for cutting off the highest diffraction orders was employed. The External Quantum Efficiency (EQE, *Y*) of the photocurrent was calculated by equation: $Y = (1240 \times j)/(I \times \lambda)$, where j is the photocurrent density (mA/cm^2), I is the incident light intensity (mW/cm^2), and λ is the wavelength (nm).

3. Results and discussion

3.1. Structure of BiSI deposits

According to the scanning electron microscopy (Fig. 2a), the prepared deposits are formed by needle-like crystallites with a length of 10–12 μm and a diameter of 0.2–0.5 μm. These crystallites grow on the FTO surface in the form of divergent beams, and a characteristic needle structure is formed. This is due to the fact that the formation of BiSI nuclei on a foreign surface (FTO) requires an additional energy, which promotes the subsequent nucleation and growth of crystallites on the already existing centers.

Analysis of the literature shows that the described needle-like structure is a feature of BiSI synthesized by various methods. In particular, the needle-shaped crystallites were observed for BiSI prepared by hydrothermal method from an aqueous solution containing thiourea, iodine, and bismuth chloride [44]. The formation of 1D crystallites is associated with the features of the structure of BiSI, in which the semiconductor is formed by "ribbon" $[(BiSI)_n]_2$ structures along [001] direction, which consist of two $(BiSI)_n$ "chains" connected by short Bi–S bonds (Fig. 2b).

XRD data (Fig. 3a) confirms the formation of one phase of bismuth thioiodide. The XRD peak positions of the BiSI film are in good agreement with JCPDS 43–0652 card corresponding to orthorhombic BiSI (*Pnam*) with the cell parameters $a = 0.851$ nm, $b = 1.026$ nm and $c = 0.417$ nm. The strongest line of BiSI film at 29.52° corresponds to (121) plane.

The selected area electron diffraction (SAED) pattern (inset in Fig. 2a) demonstrates a quasi-point shape indicating that individual 1D BiSI needles represent single crystals or contain only a limited number of single crystals. Note that the single crystalline structure of needles is inherent to BiSI prepared using various techniques: CVD [43,49], solvothermal synthesis [45], growth in gel [50].

The single-phase composition of the needle-like structure is also confirmed by the Raman spectroscopy (Fig. 3b). The Raman spectrum of BiSI deposits demonstrates 4 distinct peaks corresponding to the BiSI phase [51–53]. The peaks in the Raman spectrum have a small width (full width at half-maximum ranges from 6 to 13 cm^{-1}) indicating a high degree of structural perfection of BiSI crystallites.

The revealed microstructure of the BiSI deposit, in particular, its discontinuity (the presence of gaps between individual groups of crystals), makes it impossible the charge transport exclusively through BiSI crystallites in a plane parallel to the substrate. In other words, the formation of 1D crystallites (needle-like structures) impedes creation of BiSI based planar photodetector device.

Indirect confirmation of the single-crystalline structure of BiSI needles is their high electrical conductivity. The specific resistivity of BiSI needles estimated using the slope of their I–V curves at low voltage (below 0.1 V, Fig. 4a) and their geometrical sizes obtained from SEM experiments was found as appr. several tens of μΩ•cm. It is well known that the grain boundaries in semiconductors usually act as potential barriers impeding the carrier transport [54]. In this regard, a low resistivity of BiSI needles (by 5 order lower in comparison with single crystalline silicon typically used in microelectronics) points to a probable absence of grain boundaries in them or, at least, the absence of electrical activity of these grain boundaries.

The analysis of I–V curves shows that in the voltage range from 0.1 to 0.5 V, the quadratic dependence of current on voltage is realized (Fig. 4b). In general case, the quadratic shape of the current-voltage characteristic can be determined by the presence of intercrystalline potential barriers or the size effect in respect to the electron mean free path. However, the influence of these factors on the shape of I–V curves seems to be improbable due to limited number of grain boundaries and rather large size of crystals. The most probable reason for the quadratic shape of I–V curves is the filling of defects by electrons starting from a certain voltage value, which results in formation of a stationary space charge [55].

It is difficult to achieve good reproducibility of results (compare curves 1 and 2 in Fig. 4), when carrying out electrical measurements presented. This is due to the anisotropy of electrical conductivity of BiSI single crystals, as well as the fact that some of the needles may be broken by the metal probe, and not all of them are in a contact with probe. The last problem can be solved by using an electrolyte as contact to the array of needle-like crystals.

3.2. Photoelectrochemical properties of BiSI electrode

The synthesized BiSI deposits have a certain set of advantages. First, a low number of intercrystallite boundaries in them minimize the processes of photocharge recombination. Second, the problem of creating a second contact to each single crystal can be solved by immersing FTO/BiSI in an electrolyte solution. In this case, BiSI acts as a semiconductor photoelectrode, and the action of irradiation from the fundamental absorption region causes photoelectrochemical processes at the interface with the electrolyte. The presence of pronounced photoelectrochemical activity of BiSI in both non-aqueous [56,57] and aqueous solutions [58]

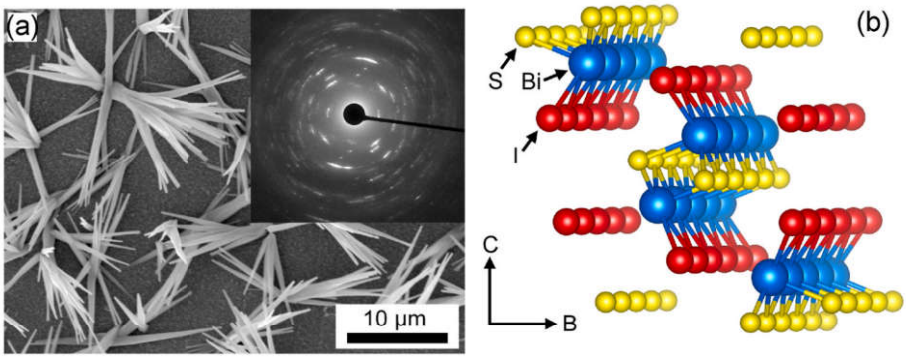

Fig. 2. SEM image and SAED (inset) of deposited BiSI crystals (a) and BiSI ball structure model (b).

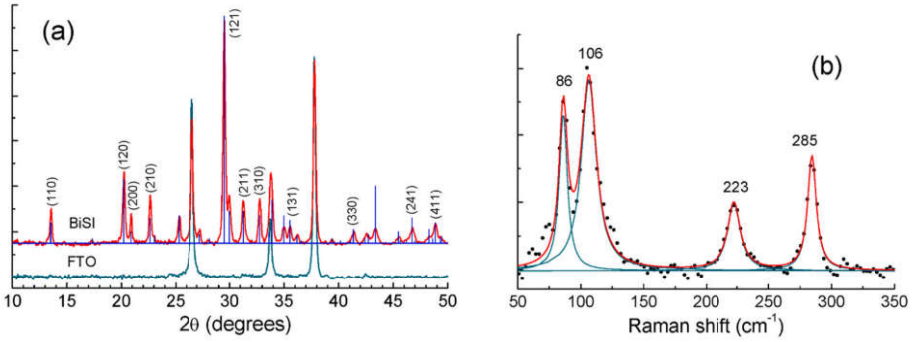

Fig. 3. XRD pattern (a) and Raman spectrum (b) for BiSI deposited on FTO substrate.

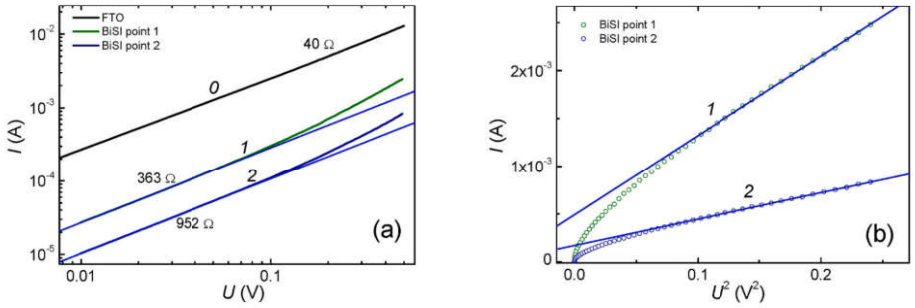

Fig. 4. Dark I–V curves of individual BiSI needles on FTO substrate when the probe is pressed to different areas of the BiSI deposit (curves 1 and 2) in various coordinates. Curve 0 is the reference one (both probes are pressed to FTO).

opens up the possibility of creating PEC detectors in the visible range of the spectrum based on it.

To substantiate the optimal operating modes of a semiconductor photodetector, it was necessary to obtain data on the mechanism and kinetics of photoelectrochemical processes in solutions with various redox systems, the dependence of the dark current on the electrode potential, as well as the spectral dependence of the quantum efficiency of the photocurrent.

Photocurrent *vs* electrode potential curves in various aqueous electrolytes for BiSI deposit are presented in Fig. 5. Taking into account a micrometer-range size of needle-like crystallites, PEC behavior of BiSI

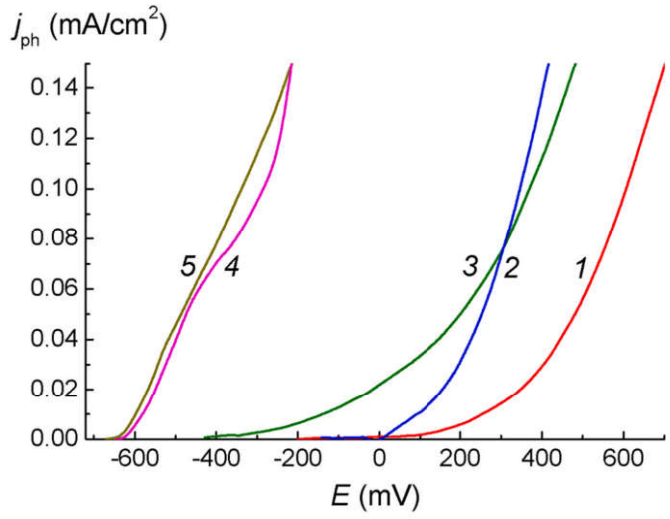

Fig. 5. Photocurrent vs. electrode potential curves for BiSI in various aqueous electrolytes: 0.5 M Na_2SO_4 (1), 0.5 M Na_2SO_3 (2), 0.05 M KI + 0.5 M Na_2SO_4 (3), 0.05 M Na_2S + 0.5 M Na_2SO_4 (4), 0.05 M KI + 0.05 M Na_2S +0.5 M Na_2SO_4 (5).

can be explained from the classical positions for bulk semiconductors [59]. The main role in the efficient separation of photogenerated electron-hole pairs is played by the electric field of the space-charge region at the semiconductor-electrolyte interface [59]. This field prevents the recombination of photogenerated charges and determines the direction of their transport either into the electrolyte or into the conductive substrate. Fig. 1 schematically shows the geometry of the movement of charges: photoholes to the interface with electrolyte, and photoelectrons along the needle to the FTO substrate.

It is known that the photocurrent onset potential in the first approximation corresponds to the flat-band potential (E_{fb}) of semiconductor [59]. An analysis of the position of the photocurrent curves on the potential scale (Fig. 5) allows us concluding that the energy bands of bismuth thioiodide shift to the region of more negative potentials when sulfide and iodide anions are added to the solution. A similar effect is described in the literature for cadmium sulfide: when sulfide anions are introduced into solution, the flat band potential E_{fb} decreases by 60 mV in the case of an increase in the S^{2-} concentration by an order of magnitude [60]. A shift of E_{fb} to the cathodic region was also observed on bismuth sulfide Bi_2S_3 nanoparticles [61]. The flat band potential shift is explained by the specific adsorption of sulfide anions, which results in a change of the potential distribution in the double electric layer and, as a consequence, a shift in the band diagram of the semiconductor [59, 61].

The shift of the energy bands of BiSI to more negative potentials contributes to an increase in the photocorrosion resistance of the semiconductor and, hence, the temporal stability of the PEC system. For this reason, all further photoelectrochemical experiments were performed using 0.05 M KI – 0.05 M Na_2S + 0.5 M Na_2SO_4 electrolyte. In this solution the nature of the anodic photocurrent is associated with the oxidation of iodide and sulfide anions (the corresponding equations are given in Fig. 1). On the counter electrode, the reverse process occurs: the reduction of molecular iodine and polysulfide anions. Fig. 6 presents a potentiodynamic polarization curve for BiSI electrode and reference FTO substrate under chopped LED illumination. As is seen, the dark

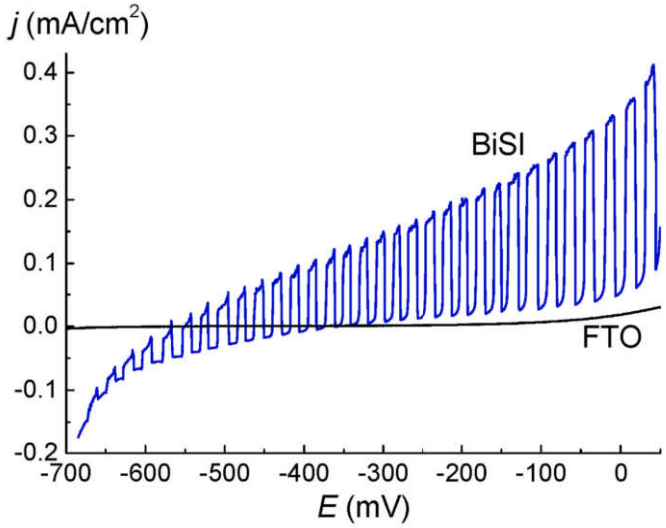

Fig. 6. Linear sweep voltammetry for BiSI electrode and reference FTO substrate under chopped LED illumination (465 nm, 1.2 mW/cm^2) in 0.05 M KI + 0.05 M Na_2S +0.5 M Na_2SO_4 aqueous electrolyte.

current is close to zero at the electrode potentials in the range from appr. −0.3 to appr. −0.4 V indicating that this potential range is the most appropriate for creation of PEC detectors providing their high detectivity.

Spectral dependence of EQE is given in Fig. 7a. Despite the fact that the conductive non-photosensitive FTO substrate is only partially covered with the BiSI deposit, the EQE is extremely high: 52 % at 400 nm. The ampere-watt responsivity calculated from EQE spectrum is given in Fig. 7b. Note that the EQE and responsivity values obtained in this work surpass the corresponding values reported for PEC detectors based on semiconducting bismuth compounds [21,56,61–65]. As noted above, such a high efficiency of the photoelectrochemical process is associated with the single-crystal needle-like structure of the deposit, which leads to a low amount of intercrystallite boundaries (barriers) that act as recombination centers. Moreover, if each particular needle-like crystal is dipped into electrolyte, the distance to be overcome by photoholes to reach the semiconductor/electrolyte interface does not exceed the radius of the needle (a few hundreds of nanometers), which results in insignificance of recombination losses (Fig. 1).

One can see a monotonic increase of EQE with the wavelength decrease. Such spectral dependence EQE is determined by two factors. First, the decrease of wavelength gives rise to the growth of light absorption in the BiSI deposit. Second, when the wavelength is decreasing, the photocharge generation area shifts to the FTO/BiSI interface, where the strength of electric field pushing holes into the electrolyte is maximal [66].

Spectral dependence of EQE was used for determination of the band gap energy (E_g) of BiSI. The most commonly used methods for E_g determination are based on the analysis of transmission or diffuse reflection spectra. However, in our case such approaches are not applicable due to discontinuity of BiSI deposits. Moreover, when analyzing transmission or diffuse reflection spectra, the determined E_g values can be distorted by other types of absorption not associated with the excitation of electrons from the valence band into the conduction band of semiconductor. Their influence on the determined E_g values can be minimized in the spectral dependence of the External Quantum Efficiency (EQE, Y). Indeed, EQE values calculated from a photocurrent spectrum can be considered as $Y(\lambda) = Y_1(\lambda) \bullet Y_2(\lambda)$, where $Y_1(\lambda)$ is the fraction of incident photons, which result in generation of electron-hole pairs, and $Y_2(\lambda)$ is the fraction of the photogenerated charge carriers participating in photoelectrochemical reactions. Near the edge of fundamental absorption, $Y_1(\lambda)$ is proportional to the absorption coefficient, and since $Y_1(\lambda)$ dependence is much stronger in comparison with $Y_2(\lambda)$, the spectral dependence of Y_2 can be neglected. Similar approach to determination of band gap energy was applied by us for cadmium telluride [67], bismuth vanadate [68], cuprous oxide [69] and bismuth oxysulfide [70,71]. The linearization of $Y(\lambda)$ dependence in the Tauc coordinates gives the band gap energy values $E_{gd} = 1.59$ eV and $E_{gi} = 1.35$ eV for direct and indirect electron transitions, respectively.

BiSI electrodes demonstrate a high specific detectivity. Assuming that the noise from the dark current gives the major contribution to the total noise [72–74], the specific detectivity can be presented as

$$D^* = \frac{R\sqrt{S}}{\sqrt{2q_e I_d}}, \tag{3}$$

where R is the ampere-watt responsivity, S is the area of the detector, q_e is the electron charge, and I_d is the dark current. From a formal point of view, at the electrode potential corresponding to the transition from the dark anodic current to the dark cathodic current, its value should be zero, and, accordingly, the specific detectivity D^* should tend to infinity. However, in these calculations it is necessary to use not the absolute value of the dark current, but the exchange current, since at zero dark current on the polarization curve, it consists of two mutually compensating cathodic and anodic currents. However, this compensation does not in any way reduce the level of fluctuations, although it gives a total zero current. In other words, shot electrochemical noise is determined by the total noise of the partial cathodic and anodic currents that make up the exchange current.

The exchange current I_0 was estimated using the charge transfer resistance value R_{ct} determined by the slope of the linear part of the dark current polarization curve at zero overvoltage. By definition,

$$R_{ct} = \frac{kT}{nq_e}\frac{1}{I_0}, \tag{4}$$

where k is the Boltzmann constant, T is the temperature, and $n = 1$.

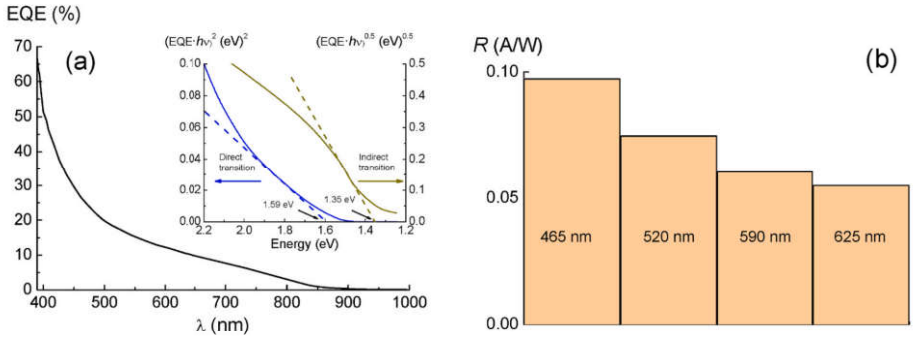

Fig. 7. EQE spectrum for BiSI electrode at $E = -300$ mV (a) and the Tauc plots for direct and indirect electron transitions (inset); ampere-watt responsivity at various wavelength (b).

The calculation from the slope of the polarization curve recorded in 0.05 M KI + 0.05 M Na_2S +0.5 M Na_2SO_4 aqueous electrolyte gives R_{ct} = 9.6•10^4 Ohm. According to Eq. (4), the exchange current is equal to 2.7•10^{-7} A. If we take this exchange current as the minimum possible dark current, R = 0.1 A/W (Fig. 7b), and S = 1 cm^2, we obtain from Eq. (3) D^* = 3.4•10^{11} cm•$Hz^{1/2}$/W. The calculated D^* significantly exceeds the corresponding values reported for PEC detectors based on semiconducting bismuth compounds (3.75•10^8 cm•$Hz^{1/2}$/W for Bi_2S_3 [62], 2.34•10^{10} cm•$Hz^{1/2}$/W for Bi_2O_2S [21]).

Chronoamperograms for BiSI electrodes under illumination with low and high intensity are presented in Fig. 8. If the intensity of the incident light is low (1 mW/cm^2), the photocurrent slowly increases with time pointing to the photoinduced deactivation of centers of charge recombination (Fig. 8a). Similar effect was observed by us for hybrid organic-inorganic perovskites [75]. In the case of high-intensity illumination (25 mW/cm^2), one can see a sharp initial growth of the photocurrent after turning on the light with a subsequent slow photocurrent decrease (Fig. 8b), which indicates that photoelectrochemical process in this case takes place in the diffusion-limited mode in electrolyte.

Fast response to the changes of incident light intensity is one of the general requirements to high-quality photodetectors. As our experiments demonstrated, the prepared BiSI electrodes are characterized by rather fast on/off time. The on-time was determined as the time interval corresponding to the increase of current to 90 % of the maximal value, whereas the off-time was determined as the time interval corresponding to the decrease of current from 100 % to 10 % of the maximal value (see horizontal black lines in Fig. 8b). The determined on/off times are equal to 26 and 435 ms, respectively, which is comparable with corresponding values for PEC detectors based on semiconducting bismuth compounds [21,29,62,63,76].

Fig. 9 demonstrates the current under cyclic illumination of the BiSI electrode. As is seen, after initial decrease of the dark current and increase of the photocurrent, the electrode demonstrates high temporal stability (thousands of cycles) under visible light illumination.

4. Conclusions

BiSI deposits with needle-like structure were grown on the surface of FTO glass substrates using one stage chemical bath deposition method from the aqueous solution containing $Bi(NO_3)_3$, thiourea, KI and HNO_3. According to the XRD and Raman analyses, the prepared deposits do not contain any additional phases. SAED analysis enables one to conclude that the grown needles represent single crystals. Low width of Raman lines points to their high crystal quality. The tendency to form 1D crystal is associated with the ribbon structure of BiSI.

To study the charge transport in these systems, we used an electrolytic contact based on aqueous solutions of Na_2S and KI. On the one hand, this makes it possible to create an almost perfect contact with each single crystal. On the other hand, the presence of sulfide and iodide anions in the solution ensures a rather negative flat band potential and photocorrosion stability of the system.

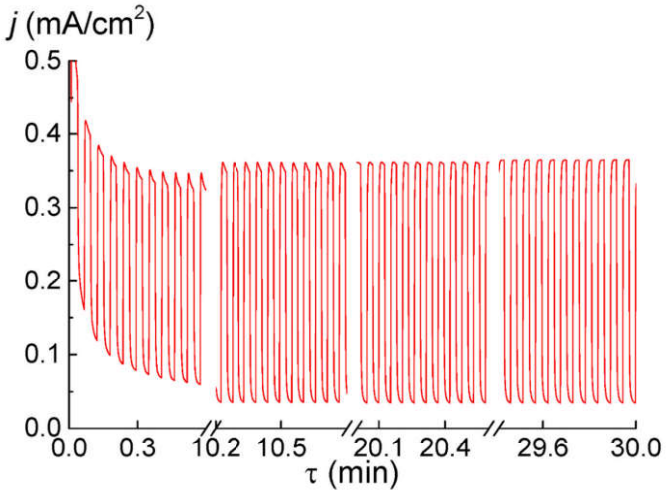

Fig. 9. Variation of the BiSI electrode current under cyclic illumination in 0.05 M KI + 0.05 M Na_2S +0.5 M Na_2SO_4 aqueous electrolyte. E = −400 mV.

The practical absence of intercrystallite boundaries in the obtained structures allows us to consider these systems as an ensemble of single-crystal photoelectrodes with high external quantum efficiency of photon-to-current conversion. As result, EQE reaches tens of percent under visible light illumination, which corresponds to responsivity up to 0.16 A/W for violet light excitation (400 nm). The specific detectivity of BiSI photoelectrode is restricted by the exchange current and is as high as 3.4•10^{11} cm•$Hz^{1/2}$/W. The PEC-type BiSI detector exhibit on/off time equal 26/435 ms, comparable with the values for other chalcohalide materials of any type. In aqueous solution containing both S^{2-} and I^- anions, the prepared photodetector is characterized by a high temporal stability of photocurrent and cyclability (thousands of cycles) under visible light illumination.

CRediT authorship contribution statement

Evgeny Bondarenko: Writing – original draft, Methodology, Investigation, Conceptualization. **Anatoly I. Kulak:** Writing – original draft, Conceptualization. **Alexander V. Mazanik:** Writing – original draft, Investigation, Conceptualization. **Ivan A. Svito:** Project administration, Investigation. **Eugene Streltsov:** Writing – original draft, Project administration, Conceptualization.

Declaration of competing interest

The authors declare that they have no known competing financial

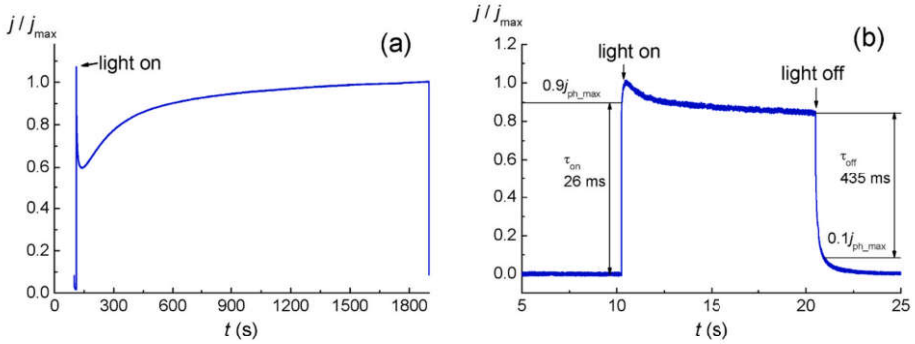

Fig. 8. Chronoamperograms for BiSI electrodes under illumination with low (a) and high (b) intensity in 0.05 M KI + 0.05 M Na_2S +0.5 M Na_2SO_4 aqueous electrolyte. E = −400 mV.

interests or personal relationships that could have appeared to influence the work reported in this paper.

Acknowledgements

E.A.B. acknowledges the Polish National Center for Research and Development [grant number SzN/I/30/Gigakwant/2022]. E.A.S. and I. A.S. acknowledge the State Research Program "Photonics and Electronics for Innovations" of the Republic of Belarus [grant number 2.2.3] for financial support. A.V.M. acknowledges the State Research Program "Energy and Nuclear Processes and Technologies" of the Republic of Belarus [grant number 1.1.02]. We acknowledge Alesya Paddubskaya for the assistance with measurements of I–V curves.

Data availability

Data will be made available on request.

References

[1] D. Schall, D. Neumaier, M. Mohsin, B. Chmielak, J. Bolten, C. Porschatis, A. Prinzen, C. Matheisen, W. Kuebart, B. Junginger, W. Templ, A.L. Giesecke, H. Kurz, 50 GBit/s photodetectors based on wafer-scale graphene for integrated silicon photonic communication systems, ACS Photonics 1 (2014) 781–784, https://doi.org/10.1021/PH5001605.

[2] D. Thomson, A. Zilkie, J.E. Bowers, T. Komljenovic, G.T. Reed, L. Vivien, D. Marris-Morini, E. Cassan, L. Virot, J.-M. Fédéli, J.-M. Hartmann, J.H. Schmid, D.-X. Xu, F. Boeuf, P. O'brien, G.Z. Mashanovich, M. Nedeljkovic, Roadmap on silicon photonics, J. Opt. 18 (2016) 073003, https://doi.org/10.1088/2040-8978/18/7/073003.

[3] K. Asakawa, Y. Sugimoto, S. Nakamura, Silicon photonics for telecom and datacom applications, Opto-Electron. Adv. 3 (2020) 200011, https://doi.org/10.29026/oea.2020.200011.

[4] Y. Takahashi, Y. Inui, M. Chihara, T. Asano, R. Terawaki, S. Noda, A micrometre-scale Raman silicon laser with a microwatt threshold, Nature 498 (2013) 470–474. https://www.nature.com/articles/nature12237.

[5] C. Wang, M. Zhang, X. Chen, M. Bertrand, A. Shams-Ansari, S. Chandrasekhar, P. Winzer, M. Lončar, Integrated lithium niobate electro-optic modulators operating at CMOS-compatible voltages, Nature 562 (2018) 101–104. https://www.nature.com/articles/s41586-018-0551-y.

[6] G. Chen, K. Chen, R. Gan, Z. Ruan, Z. Wang, P. Huang, C. Lu, A.P.T. Lau, D. Dai, C. Guo, L. Liu, High performance thin-film lithium niobate modulator on a silicon substrate using periodic capacitively loaded traveling-wave electrode, APL Photonics 7 (2022) 026103, https://doi.org/10.1063/5.0077232.

[7] M. He, M. Xu, Y. Ren, J. Jian, Z. Ruan, Y. Xu, Shengqian Gao, Shihao Sun, Xueqin Wen, Lidan Zhou, Lin Liu, Changjian Guo, Hui Chen, Siyuan Yu, Liu Liu, Xinlun Cai, High-performance hybrid silicon and lithium niobate Mach–Zehnder modulators for 100 Gbit s^{-1} and beyond, Nat. Photonics 13 (2019) 359–364. https://www.nature.com/articles/s41566-019-0378-6.

[8] N. Faramarzpour, M.M. El-Desouki, M. Jamal Deen, S. Shirani, Q. Fang, CMOS photodetector systems for low-level light applications, J. Mater. Sci. Mater. Electron. 20 (2009) 87–93, https://doi.org/10.1007/s10854-007-9455-6.

[9] J. Meng, Q. Li, J. Huang, C. Pan, Z. Li, Self-powered photodetector for ultralow power density UV sensing, Nano Today 43 (2022) 101399, https://doi.org/10.1016/J.NANTOD.2022.101399.

[10] Q. Bao, K.P. Loh, Graphene photonics, plasmonics, and broadband optoelectronic devices, ACS Nano 6 (2012) 3677–3694, https://doi.org/10.1021/NN300989G.

[11] Q. Chen, F. Gao, D.N. Wang, Z. Wang, Y. Wang, Electrically tunable optical filter based on tapered fiber coated with porous graphene film, Opt Commun. 505 (2022) 127518, https://doi.org/10.1016/j.optcom.2021.127518.

[12] J. Chen, R. Hao, S. Jin, I. Nasidi, E. Li, Photonic Moiré lattice waveguide with a large slow light bandwidth and delay-bandwidth product, Appl. Opt. 61 (2022) 5776–5781, https://doi.org/10.1364/AO.462016.

[13] C.O. Kim, S. Kim, D.H. Shin, S.S. Kang, J.M. Kim, C.W. Jang, S.S. Joo, J.S. Lee, J. H. Kim, S.H. Choi, E. Hwang, High photoresponsivity in an all-graphene p–n vertical junction photodetector, Nat. Commun. 51 (2014) 3249, https://doi.org/10.1038/ncomms4249.

[14] X. He, X. Wang, S. Nanot, K. Cong, Q. Jiang, A.A. Kane, J.E.M. Goldsmith, R. H. Hauge, F. Léonard, J. Kono, Photothermoelectric p-n junction photodetector with intrinsic broadband polarimetry based on macroscopic carbon nanotube films, ACS Nano 7 (2013) 7271–7277, https://doi.org/10.1021/nn402679u.

[15] X. Du, W. Tian, J. Pan, B. Hui, J. Sun, K. Zhang, Y. Xia, Piezo-phototronic effect promoted carrier separation in coaxial p-n junctions for self-powered photodetector, Nano Energy 92 (2022) 106694, https://doi.org/10.1016/j.nanoen.2021.106694.

[16] H. Yuan, X. Liu, F. Afshinmanesh, W. Li, G. Xu, J. Sun, B. Lian, A.G. Curto, G. Ye, Y. Hikita, Z. Shen, S.C. Zhang, X. Chen, M. Brongersma, H.Y. Hwang, Y. Cui, Polarization-sensitive broadband photodetector using a black phosphorus vertical p–n junction, Nat. Nanotechnol. 10 (2015) 707–713, https://doi.org/10.1038/nnano.2015.112.

[17] G.P. Weckler, Operation of p-n junction photodetectors in a photon flux integrating mode, IEEE J. Solid State Circ. 2 (1967) 65–73, https://doi.org/10.1109/JSSC.1967.1049795.

[18] E. Monroy, E. Muñoz, F.J. Sánchez, F. Calle, E. Calleja, B. Beaumont, P. Gibart, J. A. Muñoz, F. Cussó, High-performance GaN p-n junction photodetectors for solar ultraviolet applications, Semicond. Sci. Technol. 13 (1998) 1042, https://doi.org/10.1088/0268-1242/13/9/013.

[19] S.S. Shaker, R.A. Ismail, D.S. Ahmed, Preparation of bismuth oxide nanoplatelets/Si photodetector by laser ablation in liquid under effect of an external magnetic field, Silicon 14 (2022) 107–113, https://doi.org/10.1007/S12633-020-00789-4.

[20] S. Praveen, S. Veeralingam, S. Badhulika, A flexible self-powered UV photodetector and optical UV filter based on β-Bi_2O_3/SnO_2 quantum dots Schottky heterojunction, Adv. Mater. Interfac. 8 (2021) 2100373, https://doi.org/10.1002/ADMI.202100373.

[21] X. Yang, L. Qu, F. Gao, Y. Hu, H. Yu, Y. Wang, M. Cui, Y. Zhang, Z. Fu, Y. Huang, W. Feng, B. Li, P. Hu, High-performance broadband photoelectrochemical photodetectors based on ultrathin Bi_2O_2S nanosheets, ACS Appl. Mater. Interfaces 14 (2022) 7175–7183, https://doi.org/10.1021/acsami.1c22448.

[22] M.I. Zappia, G. Bianca, S. Bellani, N. Curreli, Z. Sofer, M. Serri, L. Najafi, M. Piccinni, R. Oropesa-Nuñez, P. Marvan, V. Pellegrini, I. Kriegel, M. Prato, A. Cupolillo, F. Bonaccorso, Two-dimensional gallium sulfide nanoflakes for UV-selective photoelectrochemical-type photodetectors, J. Phys. Chem. C 125 (2021) 11857–11866, https://doi.org/10.1021/acs.jpcc.1c03597.

[23] N.H. Harb, F.A.H. Mutlak, Effect of etching current density on spectroscopic, structural and electrical properties of porous silicon photodetector, Optik 249 (2022) 168298, https://doi.org/10.1016/j.ijleo.2021.168298.

[24] W. Tian, H. Sun, L. Chen, P. Wangyang, X. Chen, J. Xiong, L. Li, Low-dimensional nanomaterial/Si heterostructure-based photodetectors, InfoMat 1 (2019) 140–163, https://doi.org/10.1002/inf2.12014.

[25] J. Michel, J. Liu, L. Kimerling, High-performance Ge-on-Si photodetectors, Nat. Photonics 4 (2010) 527–534, https://doi.org/10.1038/nphoton.2010.157.

[26] J. Liu, J. Michel, W. Giziewicz, D. Pan, K. Wada, D.D. Cannon, S. Jongthammanurak, D.T. Danielson, L.C. Kimerling, J. Chen, F.Ö. Ilday, F. X. Kärtner, J. Yasaitis, High-performance, tensile-strained Ge p-i-n photodetectors on a Si platform, Appl. Phys. Lett. 87 (2005) 103501, https://doi.org/10.1063/1.2037200.

[27] M. Ilegems, B. Schwartz, L.A. Koszi, R.C. Miller, Integrated multijunction GaAs photodetector with high output voltage, Appl. Phys. Lett. 33 (1978) 629–631, https://doi.org/10.1063/1.90443.

[28] B.W. Jia, K.H. Tan, W.K. Loke, S. Wicaksono, K.H. Lee, S.F. Yoon, Monolithic integration of InSb photodetector on silicon for mid-infrared silicon photonics, ACS Photonics 5 (2018) 1512–1520, https://doi.org/10.1021/acsphotonics.7b01546.

[29] S.N. Hu, W. Qin, S. Jia, P. Zhang, M. Ai, S. Jin, Y. Ye, Controlled in situ synthesis of Bi_2S_3/ZnS nano film and its photoelectrochemical and photoresponsive performances, Optoelectron. Adv. Mater. - Rapid Commun. 13 (2019) 368–375.

[30] J. Xu, H. Li, S. Fang, K. Jiang, H. Yao, F. Fang, F. Chen, Y. Wang, Y. Shi, Synthesis of bismuth sulfide nanobelts for high performance broadband photodetectors, J. Mater. Chem. C 8 (2020) 2102–2108, https://doi.org/10.1039/C9TC06780A.

[31] S. Liu, Z. Huang, H. Qiao, R. Hu, Q. Ma, K. Huang, H. Li, X. Qi, Two-dimensional Bi_2Se_3 nanosheet based flexible infrared photodetector with pencil-drawn graphite electrodes on paper, Nanoscale Adv. 2 (2020) 906–912, https://doi.org/10.1039/C9NA00745H.

[32] X. Ren, W. Zheng, H. Qiao, L. Ren, S. Liu, Z. Huang, X. Qi, Z. Wang, J. Zhong, H. Zhang, Enhanced photoresponse behavior of Au@Bi_2Te_3 based photoelectrochemical-type photodetector at solid-solid-liquid joint interface, Mater. Today Energy 16 (2020) 100401, https://doi.org/10.1016/j.mtener.2020.100401.

[33] L. Su, W. Ouyang, X. Fang, Facile fabrication of heterostructure with p-BiOCl nanoflakes and n-ZnO thin film for UV photodetectors, J. Semiconduct. 42 (2021) 052301, https://doi.org/10.1088/1674-4926/42/5/052301.

[34] M.E. Kazyrevich, E.A. Streltsov, M.V. Malashchonak, A.V. Mazanik, A.I. Kulak, P. Ščajev, V. Grivickas, Crystal stacking: a route to control photoelectrochemical behavior of BiOBr films, Electrochim. Acta 290 (2018) 63–71, https://doi.org/10.1016/j.electacta.2018.09.019.

[35] M.E. Kazyrevich, M.V. Malashchonak, A.V. Mazanik, E.A. Streltsov, A.I. Kulak, C. Bhattacharya, Photocurrent switching effect on platelet-like BiOI electrodes: influence of redox system, light wavelength and thermal treatment, Electrochim. Acta 190 (2016) 612–619, https://doi.org/10.1016/j.electacta.2015.12.229.

[36] N.T. Hahn, A.J.E. Rettie, S.K. Beal, R.R. Fullon, C.B. Mullins, n-BiSI thin films: selenium doping and solar cell behavior, J. Phys. Chem. C 116 (2012) 24878–24886, https://doi.org/10.1021/jp3088397.

[37] H. Kunioku, M. Higashi, R. Abe, Low-temperature synthesis of bismuth chalcohalides: candidate photovoltaic materials with easily, continuously controllable band gap, Sci. Rep. 61 (2016) 32664, https://doi.org/10.1038/srep32664.

[38] H. Sun, G. Yang, J. Chen, C. Kirk, N. Robertson, Facile synthesis of BiSI and $Bi_{13}S_{18}I_2$ as stable electrode materials for supercapacitor applications, J. Mater. Chem. C 8 (2020) 13253–13262, https://doi.org/10.1039/D0TC02993A.

[39] I. Aguiar, M. Mombrú, M.P. Barthaburu, H.B. Pereira, L. Fornaro, Influence of solvothermal synthesis conditions in BiSI nanostructures for application in ionizing radiation detectors, Mater. Res. Express 3 (2016) 025012, https://doi.org/10.1088/2053-1591/3/2/025012.

[40] K. Mistewicz, T.K. Das, B. Nowacki, A. Smalcerz, H.J. Kim, S. Hajra, M. Godzierz, O. Masiuchok, Bismuth sulfoiodide (BiSI) nanorods: synthesis, characterization, and photodetector application, Sci. Rep. 13 (2023) 8800, https://doi.org/10.1038/s41598-023-35899-7.

[41] O. Madelung, Semiconductors: Data Handbook, third ed., Springer, 2004.

[42] S. Farooq, T. Feeney, J.O. Mendes, V. Krishnamurthi, S. Walia, E. Della Gaspera, J. Van Embden, S. Farooq, T. Feeney, J.O. Mendes, E. Della Gaspera, J. Van Embden, V. Krishnamurthi, S. Walia, High gain solution-processed carbon-free BiSI chalcohalide thin film photodetectors, Adv. Funct. Mater. 31 (2021) 2104788, https://doi.org/10.1002/adfm.202104788.

[43] D. Arivuoli, F.D. Gnanam, P. Ramasamy, Growth of bismuth sulpho-iodide single crystals from vapour, J. Mater. Sci. 21 (1986) 2835–2838, https://doi.org/10.1007/BF00551498.

[44] X. Su, G. Zhang, T. Liu, Y. Liu, J. Qin, C. Chen, A facile and clean synthesis of pure bismuth sulfide iodide crystals, Russ. J. Inorg. Chem. 51 (2006) 1864–1868, https://doi.org/10.1134/S0036023606120047.

[45] J. Lee, B.K. Min, I. Cho, Y. Sohn, Synthesis and characterization of 1-D BiSI and 2-D BiOI nanostructures, Bull. Kor. Chem. Soc. 34 (2013) 773–776, https://doi.org/10.5012/bkcs.2013.34.3.773.

[46] L. Zhu, Y. Xie, X. Zheng, X. Yin, X. Tian, Growth of compound Bi^{III}-VI^{A}-VII^{A} crystals with special morphologies under mild conditions, Inorg. Chem. 41 (2002) 4560–4566, https://doi.org/10.1021/ic025527m.

[47] W.J. Fa, P.J. Li, Y.G. Zhang, L.L. Guo, J.F. Guo, F.L. Yang, The competitive growth of BiOI and BiSI in the solvothermal process, Adv. Mater. Res. 236–238 (2011) 1919–1922. https://doi.org/10.4028/www.scientific.net/AMR.236-238.1919.

[48] G. Hodes, Chemical Solution Deposition of Semiconductor Films, CRC Press, 2002, https://doi.org/10.1201/9780203909096.

[49] D. Arivuoli, F.D. Gnanam, P. Ramasamy, Growth of SbSI and BiSI from vapour by iodine transport, Mater. Chem. Phys. 16 (1987) 181–188, https://doi.org/10.1016/0254-0584(87)90029-0.

[50] R.R. Kumar, G. Raman, F.D. Gnanam, Growth of single crystals of bismuth sulpho iodide in gel, J. Mater. Sci. 24 (1989) 4531–4534, https://doi.org/10.1007/BF00544540.

[51] R.A. Groom, A. Jacobs, M. Cepeda, R. Drummey, S.E. Latturner, Structural and optical properties of Sb-substituted BiSI grown from sulfur/iodine flux, Inorg. Chem. 56 (2017) 12362–12368, https://doi.org/10.1021/acs.inorgchem.7b01839.

[52] D. Tiwari, F. Cardoso-Delgado, D. Alibhai, M. Mombrú, D.J. Fermín, Photovoltaic performance of phase-pure orthorhombic BiSI thin-films, ACS Appl. Energy Mater. 2 (2019) 3878–3885, https://doi.org/10.1021/acsaem.9b00544.

[53] H. Sun, G. Yang, J. Chen, C. Kirk, N. Robertson, Facile synthesis of BiSI and $Bi_{13}S_{18}I_2$ as stable electrode materials for supercapacitor applications, J. Mater. Chem. C 8 (2020) 13253, https://doi.org/10.1039/d0tc02993a.

[54] W.E. Taylor, N.H. Odell, H.Y. Fan, Grain boundary barriers in germanium, Phys. Rev. 38 (1952) 867–875, https://doi.org/10.1103/PhysRev.88.867.

[55] M.A. Lampert, P. Mark, Current Injection in Solids, Academic Press, 1970.

[56] N. Hahn, J. Self, C. Buddie Mullins, BiSI micro-rod thin films: efficient solar absorber electrodes? J. Phys. Chem. Lett. 3 (2012) 1571–1576, https://doi.org/10.1021/jz300515p.

[57] H. Kunioku, M. Higashi, R. Abe, Low-temperature synthesis of bismuth chalcohalides: candidate photovoltaic materialswith easily, continuously controllable band gap, Sci. Rep. 6 (2016) 32664, https://doi.org/10.1038/srep32664.

[58] M.E. Kazyrevich, D.Y. Ivashenka, E.A. Bondarenko, E.A. Streltsov, A.I. Kulak, Synthesis and photoelectrochemical properties of bismuth thioiodide, Proc. Natl. Acad. Sci. Belarus, Chem. Ser. 54 (2019) 413–418, https://doi.org/10.29235/1561-8331-2018-54-4-413-418.

[59] Y.Y. Gurevich, Y.V. Pleskov, Chapter 4 photoelectrochemistry of semiconductors, semicond, Semimetals. 19 (1983) 255–328, https://doi.org/10.1016/S0080-8784(08)60277-X.

[60] H. Minoura, T. Watanabe, T. Oki, M. Tsuiki, Effects of dissolved Cd^{2+} and S^{2-} ions on the flatband potential of CdS electrode in aqueous solution, Jpn. J. Appl. Phys. 16 (1977) 865–866, https://doi.org/10.1143/JJAP.16.865.

[61] L.M. Peter, K.G.U. Wijayantha, D.J. Riley, J.P. Waggett, Band-edge tuning in self-assembled layers of Bi_2S_3 nanoparticles used to photosensitize nanocrystalline TiO_2, J. Phys. Chem. B 107 (2003) 8378–8381, https://doi.org/10.1021/jp030334l.

[62] W. Huang, C. Xing, Y. Wang, Z. Li, L. Wu, D. Ma, X. Dai, Y. Xiang, J. Li, D. Fan, H. Zhang, Facile fabrication and characterization of two-dimensional bismuth(III) sulfide nanosheets for high-performance photodetector applications under ambient conditions, Nanoscale 10 (2018) 2404–2412, https://doi.org/10.1039/C7NR09046C.

[63] K. Wang, H. Qiao, J. Li, X. Qi, A robust photoelectrochemical photodetectors based on the self-healing properties of Bi_2O_2S nanoplates, Appl. Surf. Sci. 565 (2021) 150444, https://doi.org/10.1016/j.apsusc.2021.150444.

[64] S.A. Patil, Y.T. Hwang, V.V. Jadhav, K.H. Kim, H.S. Kim, Solution processed growth and photoelectrochemistry of Bi_2S_3 nanorods thin film, J. Photochem. Photobiol. Chem. 332 (2017) 174–181, https://doi.org/10.1016/j.jphotochem.2016.07.037.

[65] R. Suarez, P. Nair, P. Kamat, Photoelectrochemical behavior of Bi_2S_3 nanoclusters and nanostructured thin films, Langmuir 14 (1998) 3236–3241, https://doi.org/10.1021/la9801662.

[66] J. Bisquert, G. Garcia-Belmonte, F. Fabregat-Santiago, Modelling the electric potential distribution in the dark in nanoporous semiconductor electrodes, J. Solid State Electrochem. 3 (1999) 337–347, https://doi.org/10.1007/s100080050164.

[67] A.K. Fedotov, A.A. Ronassi, V.T.T. Vi, A.V. Mazanik, O.V. Korolik, S. M. Rabchynski, G.A. Ragoisha, E.A. Streltsov, Electrical, photoelectrical, and photoelectrochemical properties of electrodeposited CdTe films subjected to high-energy irradiation, Thin Solid Films 519 (2011) 7149–7152, https://doi.org/10.1016/j.tsf.2010.12.221.

[68] M.V. Malashchonak, E.A. Streltsov, D.A. Kuliomin, A.I. Kulak, A.V. Mazanik, Monoclinic bismuth vanadate band gap determination by photoelectrochemical spectroscopy, Mater. Chem. Phys. 201 (2017) 189–193, https://doi.org/10.1016/j.matchemphys.2017.08.053.

[69] S. Shyamal, P. Hajra, H. Mandal, A. Bera, D. Sariket, A.K. Satpati, M. V. Malashchonak, A.V. Mazanik, O.V. Korolik, A.I. Kulak, E.V. Skorb, A. Maity, E. A. Streltsov, C. Bhattacharya, Eu modified Cu_2O thin films: significant enhancement in efficiency of photoelectrochemical processes through suppression of charge carrier recombination, Chem. Eng. J. 335 (2018) 676–684, https://doi.org/10.1016/j.cej.2017.11.004.

[70] E.A. Bondarenko, E.A. Streltsov, M.V. Malashchonak, A.V. Mazanik, A.I. Kulak, E. V. Skorb, Giant incident photon-to-current conversion with photoconductivity gain on nanostructured bismuth oxysulfide photoelectrodes under visible-light illumination, Adv. Mater. 29 (2017) 1702387, https://doi.org/10.1002/adma.201702387.

[71] E. Bondarenko, P. Chulkin, M. Krzywiecki, Bismuth oxysulfide films with giant external quantum efficiency: Investigation of photoelectrochemical properties and stability in dimethyl sulfoxide solutions for application in photodetectors, Appl. Surf. Sci. 654 (2024) 159500, https://doi.org/10.1016/j.apsusc.2024.159500.

[72] W. Choi, M.Y. Cho, A. Konar, J.H. Lee, G.-B. Cha, S.C. Hong, S. Kim, J. Kim, D. Jena, J. Joo, S. Kim, High-detectivity multilayer MoS_2 phototransistors with spectral response from ultraviolet to infrared, Adv. Mater. 24 (2012) 5832–5836, https://doi.org/10.1002/adma.201201909.

[73] W. Zhang, M.H. Chiu, C.H. Chen, W. Chen, L.J. Li, A.T.S. Wee, Role of metal contacts in high-performance phototransistors based on WSe_2 monolayers, ACS Nano 8 (2014) 8653–8661, https://doi.org/10.1021/nn503521c.

[74] J. Chu, F. Wang, L. Yin, L. Lei, C. Yan, F. Wang, Y. Wen, Z. Wang, C. Jiang, L. Feng, J. Xiong, Y. Li, J. He, High-performance ultraviolet photodetector based on a few-layered 2D $NiPS_3$ Nanosheet, Adv. Funct. Mater. 27 (2017) 1701342, https://doi.org/10.1002/adfm.201701342.

[75] N.S. Mahon, O.V. Korolik, M.V. Khenkin, G.E. Arnaoutakis, Y. Galagan, V. Soriūtė, D. Litvinas, P. Ščajev, E.A. Katz, A.V. Mazanik, Photoluminescence kinetics for monitoring photoinduced processes in perovskite solar cells, Sol. Energy 195 (2020) 114–120, https://doi.org/10.1016/j.solener.2019.11.050.

[76] J. Chao, S. Xing, Y. Zhao, S. Gao, Q. Song, L. Guo, D. Wang, T. Zhang, Bismuth sulfide nanoflakes and nanorods as high performance photodetectors and photoelectrochemical cells, Solid State Sci. 61 (2016) 51–57, https://doi.org/10.1016/j.solidstatesciences.2016.09.002.